Available online at www.sciencedirect.com
ScienceDirect
Trans. Nonferrous Met. Soc. China 25(2015) 1341−1351
Transactions of Nonferrous Metals Society of China
www.tnmsc.cn

Oxidation behavior of high-entropy alloys $Al_xCoCrFeNi$ (x=0.15, 0.4) in supercritical water and comparison with HR3C steel

Yi-xuan LIU, Cong-qian CHENG, Jian-lu SHANG, Rui WANG, Peng LI, Jie ZHAO

School of Materials Science and Engineering, Dalian University of Technology, Dalian 116085, China

Received 17 May 2014; accepted 13 July 2014

Abstract: The oxidation behaviors of high-entropy alloys $Al_xCoCrFeNi$ (x=0.15, 0.4) in supercritical water at 550 and 600 °C were studied, and compared with HR3C steel. All oxide films formed on alloys are composed of spinel type $(Fe, Cr)_3O_4$ oxides. Compared with the oxide film on HR3C steel, thinner oxide films with smaller size of oxide particles were realized on $Al_{0.15}CoCrFeNi$ and $Al_{0.4}CoCrFeNi$, indicating a superior oxidation resistance of $Al_{0.15}CoCrFeNi$ and $Al_{0.4}CoCrFeNi$ to HR3C steel. Electrochemical test results reveal that surface oxide films greatly affect the electrochemical corrosion behavior of the oxidized alloys in 3.5% NaCl solution. The relatively high corrosion resistance of oxidized $Al_{0.15}CoCrFeNi$ and HR3C is attributed to the formation of thick and multi-layer oxides.

Key words: high-entropy alloy; high temperature oxidation; polarization; electrochemical impedance spectroscopy (EIS)

1 Introduction

In recent years, a novel alloy design concept based on the multi principal elements has been proposed by YEH et al [1]. Compared with conventional alloys, high-entropy alloys are composed of five or more principal elements whose concentrations are with a near equimolar ratio to the alloys. It was confirmed that high-entropy alloys possessed simple solid−solution structure rather than complex phases or intermetallic compounds due to the high mixing entropies and accompanied sluggish cooperative diffusion [2], which avoids the brittleness of compounds. Based on the contribution of above structural and compositional features, good properties such as strength, good thermal stability and oxidation were reported for high-entropy alloys [3−6].

With the demand for efficiency increase in ultra-supercritical (USC) boiler which is achieved principally through improving steam temperature and pressure, a more severe environment for boiler materials is created. Excellent high temperature mechanical properties and oxidation resistance are necessary for materials worked under such environment. Heat resistance steel HR3C (25Cr−20Ni−Nb−N) is a typical alloy used as pipe material in USC boiler superheater and reheater. To satisfy the working parameters under the new generation of USC boiler, developing new materials with outstanding properties is demanded. It was reported that high-entropy alloys exhibited excellent air oxidation resistance [6,7]. This fact suggests that the high-entropy alloys may become one of the most interesting materials that can be used in supercritical environment. Unfortunately, to the best knowledge no studies have been reported on the oxidation of high-entropy alloys in supercritical water.

Among the high-entropy alloys, $Al_xCoCrFeNi$ (x is molar ratio) has been one of the most thoroughly studied alloys until now. Higher hardness and lower diffusion rate of elements were achieved due to Al addition [8−10], therefore, improved oxidation resistance may be expected. Furthermore, addition of Al element can decrease the usage of noble metal and thus decrease the cost of alloy. In the present study, the oxidation behavior of high-entropy alloys $Al_xCoCrFeNi$ (x=0.15, 0.4) in supercritical water was examined and compared with that of HR3C steel.

It is generally recognized that the oxidation resistance in supercritical water is strongly determined by the properties of oxide film formed on the metal surface. A large number of investigations have been

Foundation item: Projects (51134013, 51171037, 51101024) supported by the National Natural Science Foundation of China
Corresponding author: Jie ZHAO; Tel: +86-411-84709076; E-mail: jiezhao@dlut.edu.cn
DOI: 10.1016/S1003-6326(15)63733-5

devoted to the identification of the thickness, composition and structure of the oxide film [11−14]. Unfortunately, the oxide film formed in supercritical water within short oxidation period is difficult to characterize using conventional inspection techniques such as mass measurement due to its small film thickness. Therefore, how to evaluate the thin oxide film is of importance in materials design and manufacturing. SUN et al [15] found that the electrochemical tests of oxide films including potentiodynamic polarization tests and electrochemical impedance spectroscopic tests (EIS) are related to the property of oxide layers, which can present the protectiveness of oxide films. Therefore, the phase composition, morphologies and chemical composition of the oxide films formed on the surface of $Al_xCoCrFeNi$ (x=0.15, 0.4) and HR3C are our focus in the present study. And electrochemical test after oxidation is also conducted to illustrate the property characteristic of oxide layers.

2 Experimental

2.1 Sample preparation and oxidation experiments

The high-entropy alloy ingots with nominal composition of $Al_xCoCrFeNi$ (x=0.15, 0.4) in molar ratio were prepared by vacuum induction smelting and casting method. The purity of each raw elemental metal was 99.9%. Approximately 1.8 kg raw materials were melted in water-cooled copper mold under pure argon (Ar) atmosphere. To ensure homogeneity, all ingots were re-melted at least five times. The alloys with different Al contents are hereafter denoted by $Al_{0.15}$ and $Al_{0.4}$.

Oxidation samples of $Al_{0.15}$, $Al_{0.4}$ and HR3C with dimensions of 10 mm×7 mm×1 mm were used in this study. They were ground to 2000 grit, followed by polish with 1.5 μm diamond paste and ultrasonic cleaning in acetone.

All oxidation experiments were performed in a 1 L autoclave. Prior to oxidation, the water was deaerated by keeping the air vent line open for 3 min while samples were kept at 200−250 °C, and the oxygen concentration of above water could be controlled under 3×10^{-6}. After deaerating, water and samples were heated up to the designed temperature and pressure, and then the oxidation experiments began. $Al_{0.15}$ and $Al_{0.4}$ were oxidized at 550 and 600 °C under 23 and 25.5 MPa for 70 h, respectively. For comparison, oxidation of HR3C specimen was performed at 600 °C under 23 MPa for 70 h.

2.2 Oxides analysis

The morphology and chemical composition of oxides were examined by SEM equipped with EDS. Phase analysis was performed by the synchrotron radiation-grazing incidence X-ray diffraction (SR-GIXRD) and laser Raman spectra (LRS).

SR-GIXRD with a large flux of the synchrotron X-ray and high resolution was carried out at the 1W1A scattering station on the 1W1 beam-line of the Beijing synchrotron radiation facility (BSRF). The wavelength and energy range were 0.1547 nm and 13.9−8.05 keV, respectively. For LRS, a fine laser beam (diameter: 1 μm) of visible rays (wavelength: 632.8 nm) was irradiated onto the specimen surface.

2.3 Electrochemical tests

Electrochemical experiments were performed on a CS350 electrochemical system. A saturated calomel electrode (SCE) was used as a reference electrode. All electrochemical tests were conducted in 3.5% NaCl solution at 25 °C. The potentiodynamic polarization tests were conducted with a potential scan rate of 0.5 mV/s and electrochemical impedance spectroscopic tests (EIS) were carried out in a frequency range of 10^{-2}−10^{5} using a 10 mV amplitude sinusoidal voltage.

3 Results and discussion

3.1 Microstructures of $Al_{0.15}$ and $Al_{0.4}$ before oxidation

The XRD patterns for $Al_{0.15}$ and $Al_{0.4}$ substrates are presented in Fig. 1. It is clear that all alloys form FCC solid solution, which can also be observed in Ref. [16].

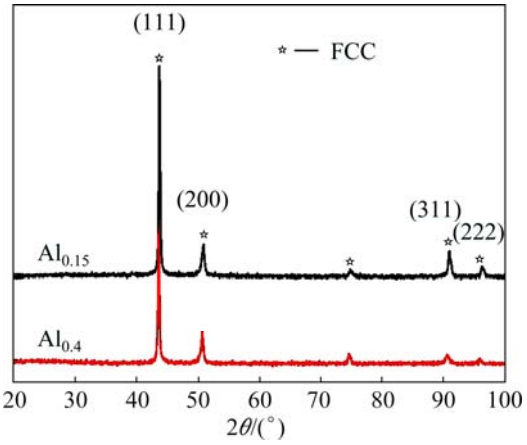

Fig. 1 XRD patterns for $Al_{0.15}$ and $Al_{0.4}$ substrates

Figure 2 shows the SEM images of $Al_{0.15}$ and $Al_{0.4}$ before oxidation. It is noted that $Al_{0.15}$ and $Al_{0.4}$ are composed of cellular crystal structure. The grain size of $Al_{0.15}$ is larger than that of $Al_{0.4}$, while the grain boundary is finer. Table 1 gives the chemical compositions of $Al_{0.15}$ and $Al_{0.4}$, which are determined by EDS. Different element distributions in these alloys are observed. For $Al_{0.15}$, there is no significant variation in the element distribution between grain boundary and bulk grain region. For $Al_{0.4}$, Al and Ni elements segregate

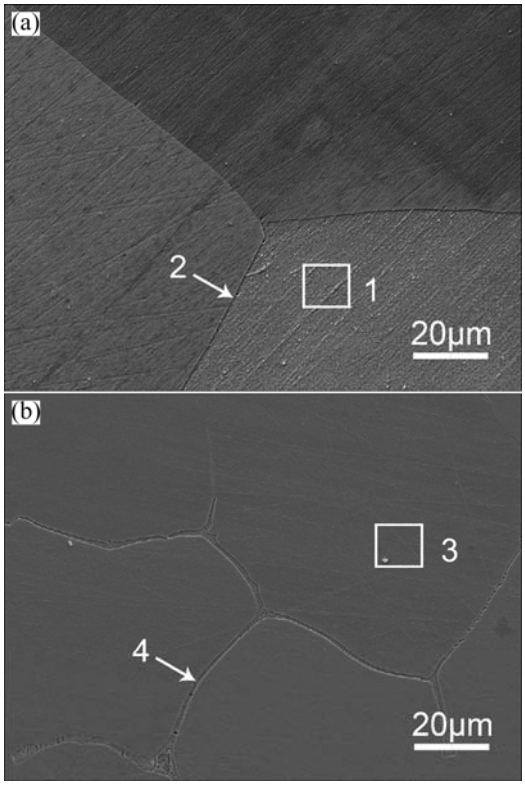

Fig. 2 SEM images of $Al_{0.15}$ (a) and $Al_{0.4}$ (b) substrates

Table 1 Chemical compositions of as-received $Al_{0.15}$ and $Al_{0.4}$ shown in Fig. 2

Area No.	Mole fraction/%				
	Al	Fe	Cr	Ni	Co
1	4.60	23.63	24.51	23.86	23.40
2	5.30	22.53	26.05	24.32	21.80
3	9.42	23.11	22.87	22.58	22.02
4	25.93	12.31	9.95	35.14	16.67

preferentially to the grain boundary region, while Fe and Cr elements prefer to the bulk grain region.

3.2 Morphology and chemical composition of oxide films on $Al_{0.15}$ and $Al_{0.4}$

The morphologies of oxide films formed on $Al_{0.15}$ and $Al_{0.4}$ at 550 and 600 ºC under 25.5 MPa for 70 h are shown in Fig. 3. In all cases, the surfaces of alloys are mostly covered by loosely packed polyhedral crystallites in Area 3 and uniform fine oxide particles in Area 4. According to the EDS analyses, these kinds of oxides vary compositions; the polyhedral crystallites are rich in Cr, while fine oxides contain high levels of Ni and Al (Table 2). The above distribution of elements is close to that of bulk grain and grain boundary regions (Table 1), indicating that the oxidation between bulk grain and grain boundary is quite inhomogeneous. Additionally, after oxidation at 600 °C, oxide films consisting of more loosened oxides are formed on both alloys and the sizes of oxide particles become larger.

Figure 4 represents the XRD patterns for $Al_{0.15}$ and $Al_{0.4}$ after oxidation at 550 °C under 25.5 MPa for 70 h. It is noted that spinel type M_3O_4 oxides are present on both surfaces of $Al_{0.15}$ and $Al_{0.4}$. Since the XRD patterns of spinels concerning Fe, Cr and Ni have similar lattice parameter, and the spinel type cannot be clarified.

Further analysis identifying the composition of oxides is presented in Fig. 5, which shows the Raman spectra of oxide films formed on $Al_{0.15}$ and $Al_{0.4}$. The presence of Fe_3O_4 (302, 513, 663 cm^{-1}), $FeCr_2O_4$ (600, 681 cm^{-1}) and $NiFe_2O_4$ (344, 486, 573, 700 cm^{-1}) is clearly visible [17,18], but the fine oxides enriched in Al are barely detectable in the oxidation products of $Al_{0.4}$. This may be due to the little concentration of the oxides enriched in Al. Combining the EDS results and phase results, it can be summarized that the oxides in bulk grain may be composed of Fe_3O_4 and $FeCr_2O_4$, while that at grain boundary consists of $NiFe_2O_4$.

3.3 Electrochemical tests of oxidized alloys

To make clear the structure and property of oxide films, EIS was performed for oxidized alloys. Figure 6 displays the experimental and simulated EIS results for $Al_{0.15}$ and $Al_{0.4}$ after oxidation at 550 and 600 °C under 25.5 MPa for 70 h. It is obvious that the EIS plots are characterized by different behaviors for these two alloys. In terms of $Al_{0.15}$, two poorly defined time constants can be identified by the two peaks in the Bode-phase plots, as represented in Fig. 6 (b), which evinces the presence of a duplex oxide film on $Al_{0.15}$. For $Al_{0.4}$, the only one time constant shown in Fig. 6 (d) is related to the single-layer structure of oxide film.

According to the EIS results obtained for the two alloys, the equivalent circuit with two time constants as shown in Fig. 7(a) was used to fit the EIS data of $Al_{0.15}$, where the high frequency time constant (R_1, CPE_1) and low frequency time constant (R_2, CPE_2) characterize the property of outer layer and inner layer, respectively. For $Al_{0.4}$, the circuit, shown in Fig. 7(b), was used. This model is widely used for the fit of a single film. R_1 and CPE_1 correspond to the resistance and capacitance of oxide film, respectively.

All the parameters fitted by the two models are listed in Table 3. A good agreement between the experimental data and fitted data is obtained. As shown in Table 3, the R_1 of oxide films on $Al_{0.4}$ shows a nobler value at higher oxidation temperatures. This indicates that the oxide film formed at 600 °C is thicker than that formed at 550 °C. The same conclusion can be drawn for $Al_{0.15}$. The $Al_{0.15}$ oxidized at 600 °C shows higher R_1 and R_2, reflecting the formation of thicker inner and outer layers. In addition, the inner oxide film of $Al_{0.15}$ exhibits a much larger resistance compared with the outer layer.

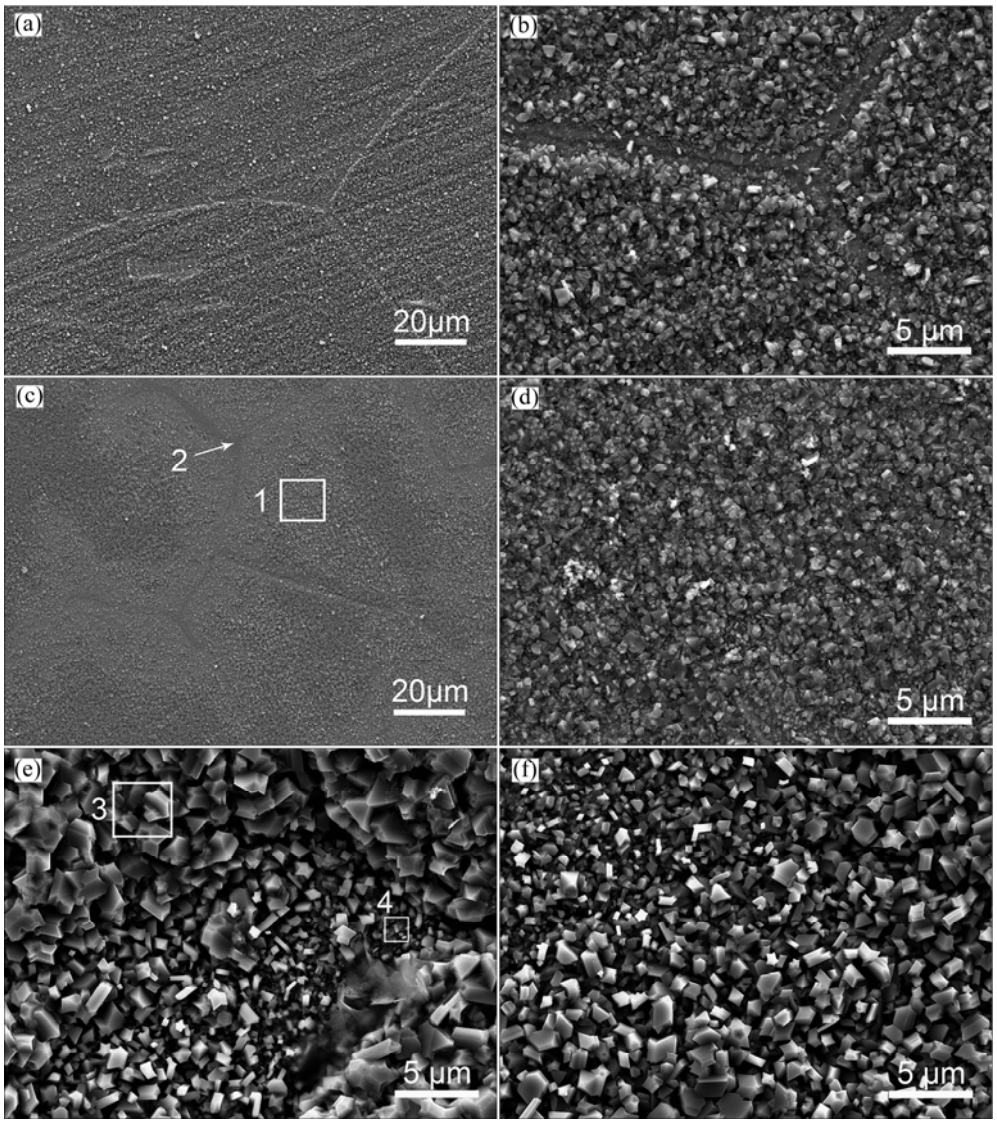

Fig. 3 Surface morphologies of oxide films formed on surfaces of alloys after 70 h oxidation under 25.5 MPa: (a, b) $Al_{0.15}$ at 550 °C; (c, d) $Al_{0.4}$ at 550 °C; (e) $Al_{0.15}$ at 600 °C; (f) $Al_{0.4}$ at 600 °C

Table 2 EDS analyses of oxide films shown in Fig. 2

Area No.	Mole fraction/%					
	O	Fe	Cr	Al	Ni	Co
1	54.65	13.55	10.82	3.18	6.63	11.16
2	32.47	8.40	8.20	19.04	20.89	11.00
3	60.01	9.66	20.55	–	–	9.78
4	45.18	9.81	17.71	3.46	14.07	9.77

This suggests that the oxidation protection is dominated by the inner layer.

The polarization curves for the substrate and oxidized $Al_{0.15}$ and $Al_{0.4}$ at 550 and 600 °C under 25.5 MPa for 70 h are presented in Fig. 8. According to the work of SUN et al [15], the self-corrosion current density (J_{corr}), self-corrosion potential (φ_{corr}) and polarization resistance (R_p) obtained by polarization curve of oxide

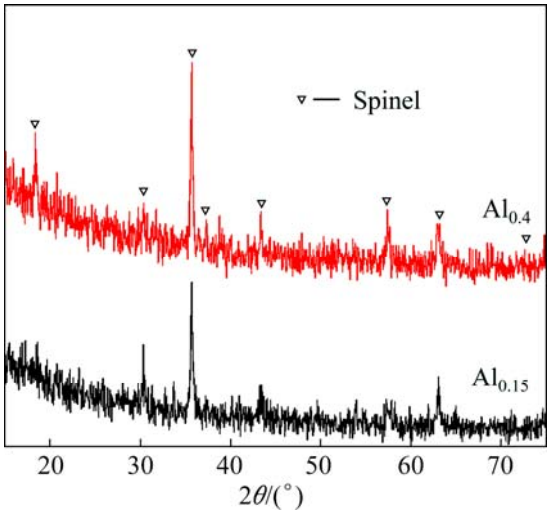

Fig. 4 XRD patterns for $Al_{0.15}$ and $Al_{0.4}$ after oxidation at 550 °C under 25.5 MPa for 70 h

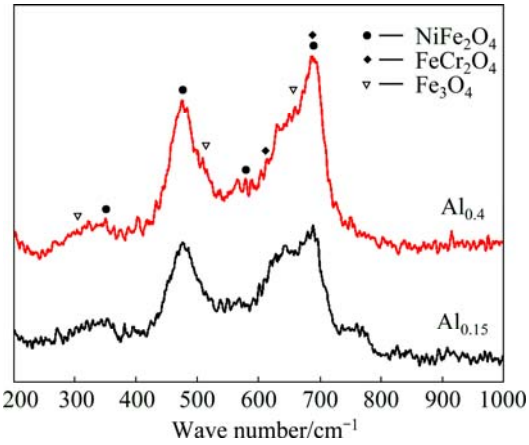

Fig. 5 Raman spectra for $Al_{0.15}$ and $Al_{0.4}$ after oxidation at 550 °C under 25.5 MPa for 70 h

films can reflect the property of oxide film. And polarization resistance is determined by the Stern−Geary equation [19]:

$$J_{corr}=\{b_a b_c/[2.303(b_a+b_c)]\}/R_p \quad (1)$$

where b_a and b_c are the Tafel slopes, and R_p is the polarization resistance. The calculated results are summarized in Table 4.

It can be seen that the R_p values of $Al_{0.15}$ and $Al_{0.4}$ are improved when these two alloys are coated with the oxides formed at 550 °C compared with that of substrate. This observation indicates that the oxides can act as a barrier, which prevents the release of metal ions from substrate to electrolyte. In contrast, the alloys oxidized at 600 °C show a lower R_p compared with that oxidized at 550 °C, suggesting a poorer protectiveness of oxides

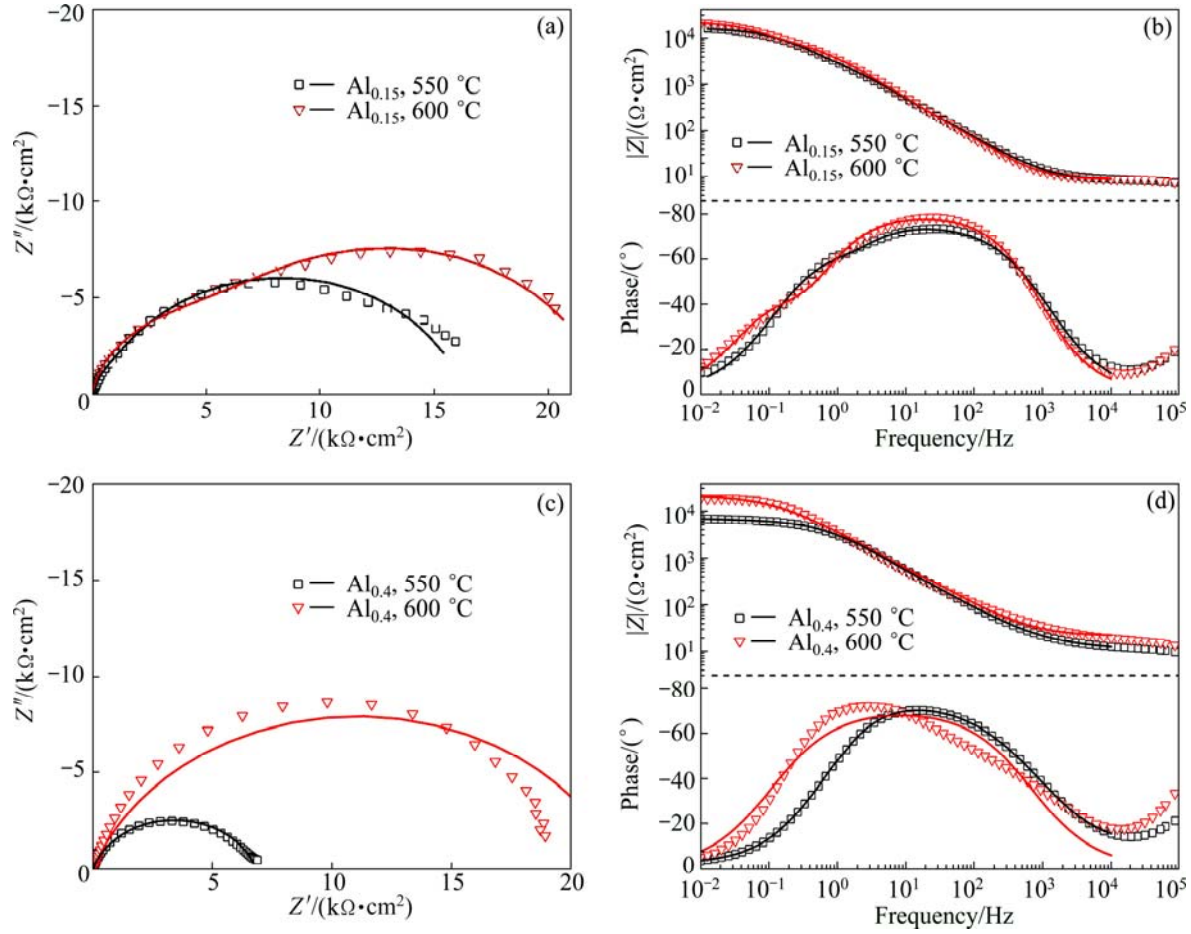

Fig. 6 EIS plots of $Al_{0.15}$ and $Al_{0.4}$ after oxidation at 550 and 600 °C under 25.5 MPa for 70 h

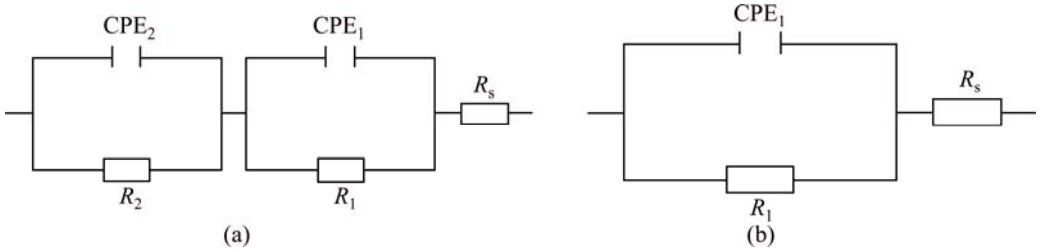

Fig. 7 Equivalent circuit used to fit EIS data: (a) $Al_{0.15}$; (b) $Al_{0.4}$

Table 3 Fitting parameters for EIS shown in Fig. 6

Sample	Temperature/°C	R_1/(Ω·cm^2)	Q_1/(μF·cm^{-2})	n_1	R_2/(Ω·cm^2)	Q_2/(μF·cm^{-2})	n_2
$Al_{0.15}$	550	388.1	176.3	0.995	15945	16.20	0.824
	600	5054	31.12	0.916	17399	58.95	0.866
$Al_{0.4}$	550	6819	11.45	0.813	–	–	–
	600	22089	10.65	0.790	–	–	–

Table 4 J_{corr}, φ_{corr} and R_p from polarization curves for substrate and oxidized $Al_{0.15}$ and $Al_{0.4}$

Sample	Temperature/°C	J_{corr}/(μA·cm^{-2})	φ_{corr}/mV	b_c/(mV·dec^{-1})	b_a/(mV·dec^{-1})	R_p/(kΩ·cm^{-2})
Substrate		1.187	−182.1	137.6	127.7	24.23
$Al_{0.15}$	550	2.308	−307.9	215.9	1071	33.80
	600	8.685	−221.5	393.4	477.3	10.78
Substrate		8.696	−195.2	483.8	389.2	10.77
$Al_{0.4}$	550	2.197	−424.3	251.7	295.6	26.87
	600	8.106	−305.0	531.7	1076	19.06

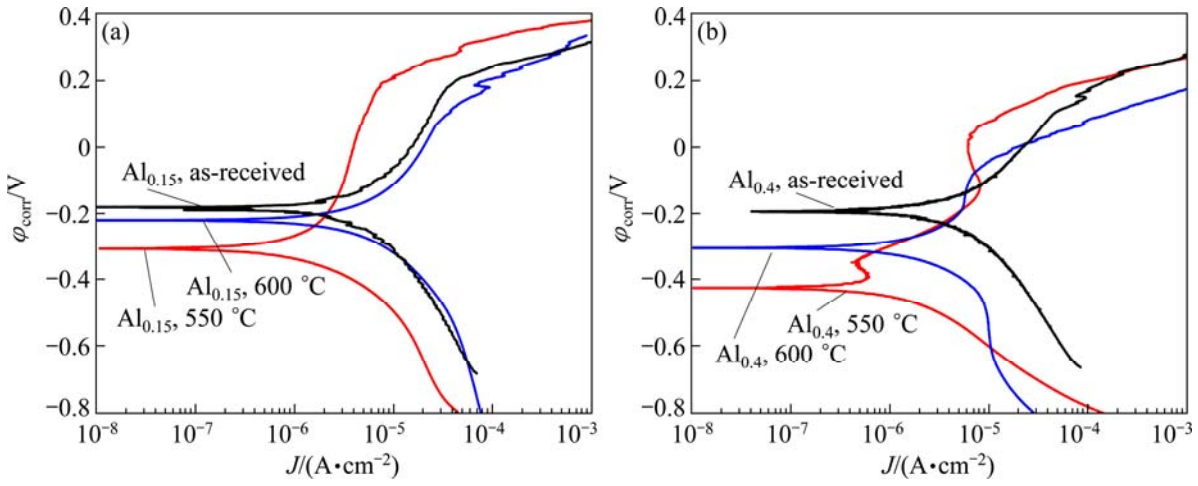

Fig. 8 Polarization curves for substrates, $Al_{0.15}$ and $Al_{0.4}$ oxidized at 550 and 600 °C under 25.5 MPa for 70 h: (a) $Al_{0.15}$; (b) $Al_{0.4}$

formed at 600 °C. This result is related to the formation of more loose oxides, which leads to the lower energy required for Cl^- ion movement across the oxides and more ions arrive to substrate.

3.4 Comparison with HR3C

A comparison of surface morphologies of $Al_{0.15}$, $Al_{0.4}$ and HR3C after oxidation at 600 °C under 23 MPa for 70 h is shown in Fig. 9. Dense oxide films with polyhedral oxides are revealed on all alloys. Such morphologies are quite similar to that of Fe_3O_4 formed on P92 alloy in supercritical water at 550−600 °C and 25 MPa [20]. And, the size of oxides formed on HR3C is larger than that on $Al_{0.15}$ and $Al_{0.4}$.

The SEM/EDS line scan analyses at the cross-section of the surfaces of $Al_{0.15}$, $Al_{0.4}$ and HR3C are presented in Fig. 10. Different characteristics of oxide layers can be observed. In terms of $Al_{0.15}$, a typical duplex oxide structure is detected, consisting of a Cr-rich inner layer and a Fe-rich outer layer. This distribution of elements is related to their affinities for oxygen and outward diffusion rates in the oxide scale. The Fe-rich inner layer is formed by the outward Fe diffusion, suggesting that the transport of Fe is noticeably higher than that of Cr. In contrary, Cr-rich inner layer reflects the preferential oxidation of this element and its slower transport rate through inner oxide. Similar duplex oxide structure with localized scale separation along the interface between two layers is revealed for HR3C. This kind of separation may result in the overheating of local region, due to the decrease in local heat transfer. Additionally, the oxide film formed on HR3C (5.4 μm) is over twice thicker than that on $Al_{0.15}$ (2.5 μm), which reflects a higher oxidation resistance of $Al_{0.15}$ than that of HR3C. This difference of thickness can be discussed from the specificity of high-entropy alloys. Different from conventional alloys, high-entropy alloys with highly concentrated solute atoms have benefit to resist

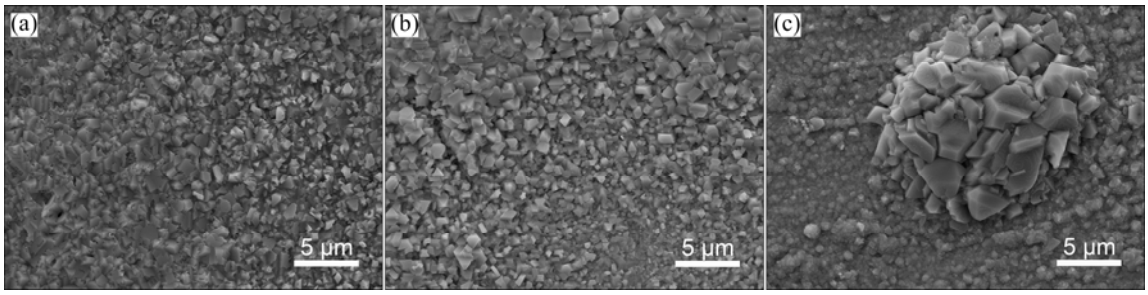

Fig. 9 Surface morphologies of oxide films formed on surfaces of alloys after 70 h oxidation at 600 °C under 23 MPa: (a) $Al_{0.15}$; (b) $Al_{0.4}$; (c) HR3C

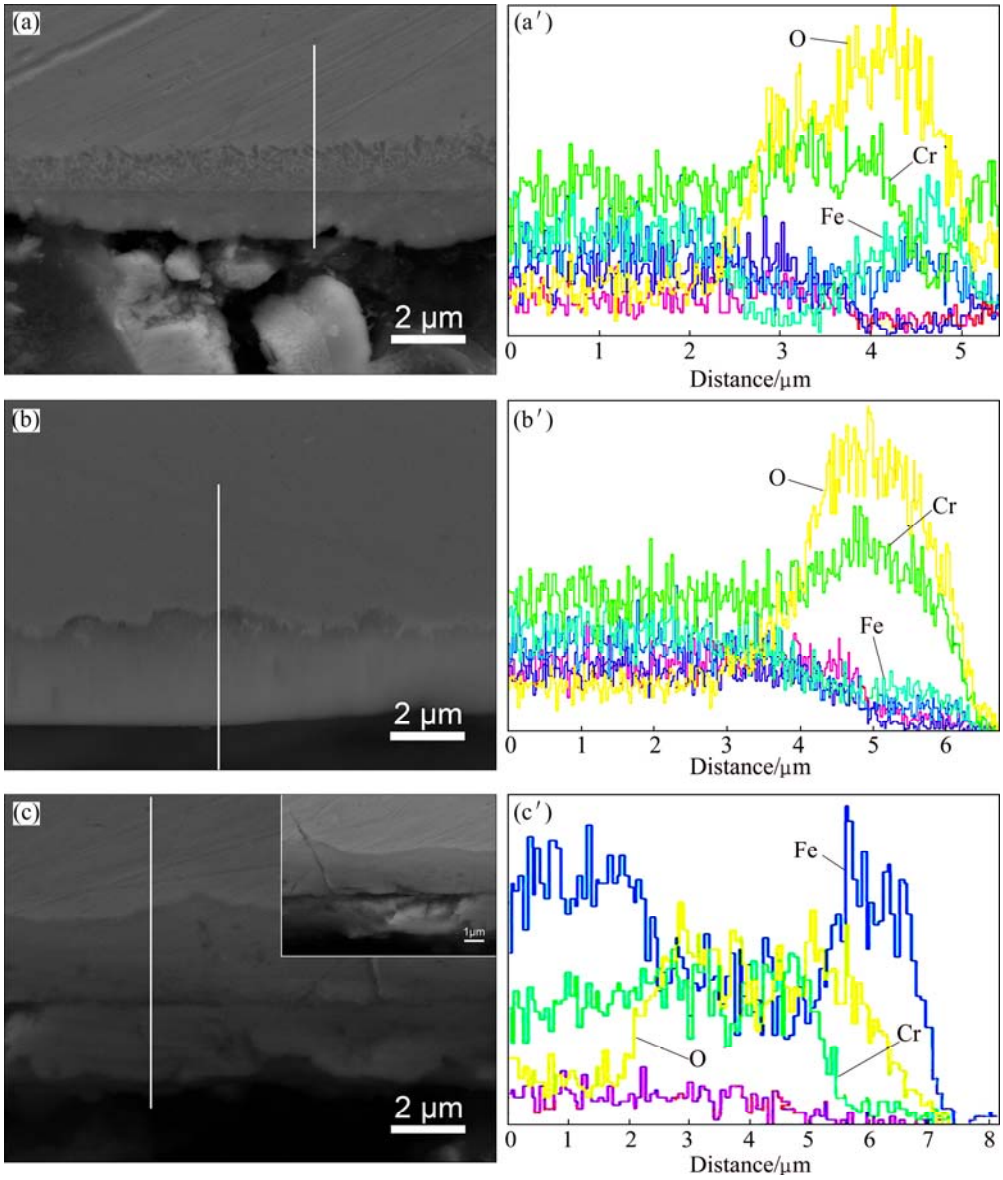

Fig. 10 SEM images (a, b, c) and EDS line scans (a′, b′, c′) at cross-section of surfaces of alloys after 70 h oxidation at 600 °C under 23 MPa: (a, a′) $Al_{0.15}$; (b, b′) $Al_{0.4}$; (c, c′) HR3C

dissolution and diffusion of metallic elements in the matrix [10]. The sluggish diffusion effect of high-entropy alloys has been verified by a series of studies [1,21]. YEH et al [1] found that the diffusion coefficients of high-entropy alloys are much smaller than those of stainless steels. Therefore, the thinner oxide film formed and higher oxidation resistance of $Al_{0.15}$ resulted from the lower diffusion rates of elements.

Different from above two alloys, only a single Cr-rich layer forms on $Al_{0.4}$. This change in the structure of oxide film indicates an improvement of oxidation resistance of $Al_{0.4}$, and it is affected by the composition change of alloys. Among the main elements of $Al_{0.15}$ and $Al_{0.4}$, Al and Cr are two possible elements to improve the oxidation resistance. It is shown from Table 1 that $Al_{0.4}$ contains lower Cr and higher Al content compared with $Al_{0.15}$. Therefore, the increase in oxidation resistance of $Al_{0.4}$ is related to the higher Al content. According to the previous works [21−24], the lattice distortion in alloys becomes more serious with the Al content increasing, and consequently the atomic movement is hindered and diffusion rate of element is reduced. According to YIN et al [20], the outer Fe oxide layer forms by outward diffusion of Fe across formed Cr/Fe-mixed oxide layer. Therefore, the outer Fe oxide layer failed to develop on $Al_{0.4}$ for 70 h oxidation because of the low diffusion rate of Fe, and only a single Cr-rich oxide layer can be observed on the surface of $Al_{0.4}$.

Figure 11 shows XRD patterns for $Al_{0.15}$, $Al_{0.4}$ and HR3C after oxidation at 600 °C under 23 MPa for 70 h. It is noted that all oxide films are composed of spinel oxides. Combined with the results of EDS line scan, the oxide scales on $Al_{0.15}$ and HR3C mainly consist of a Fe_3O_4 spinel outer layer and a $FeCr_2O_4$ spinel inner layer, while that on $Al_{0.4}$ is composed of a single $FeCr_2O_4$ layer. In addition, no oxides containing Al can be identified by XRD patterns in the oxidation products of $Al_{0.15}$ and $Al_{0.4}$. This may be related to the following reasons. According to the work of TANG et al [25], the minimum amount of Al required in alloys for forming Al_2O_3 scale is affected by the environmental partial pressure of oxygen gas, and the minimum amount of Al increases with environmental oxygen partial pressure. For supercritical water, the oxygen partial pressure is significantly increased by the high pressure environment, in which the oxygen is produced by the decomposition of water [26]. Therefore, the minimum amount of Al for forming Al_2O_3 may be higher, and no oxides containing Al form. On the other hand, the scale fails to develop an Al_2O_3 layer when water vapour is present [27,28]. It is attributed to the decrease in scale adhesion. Any cracking of the scale would allow ingress of water vapour with the formation of weak Al—OH^- bond, and then the oxide scale spalls. In terms of supercritical water, its diffusion coefficient is significantly higher than that of subcritical water [26], leading to a faster ingress of water and a more difficult development of Al_2O_3 layer.

All oxidized $Al_{0.15}$, $Al_{0.4}$ and HR3C were also analyzed by EIS to further study the structure and property of oxide films, as shown in Fig. 12. Two time constants can be found for the EIS plots of $Al_{0.15}$ and HR3C while a single time constant is found for that of $Al_{0.4}$. This result further corroborates the bilayer and single-layer structure of the oxides obtained from the SEM (Fig. 10), respectively. Table 5 summarizes the fitting parameters for EIS using the equivalent circuits shown in Fig. 7. According to the comparison between R_1 and R_2 of $Al_{0.15}$ and HR3C that are coated with duplex oxide films, the latter shows a lower R_1 and higher R_2 than those of the former. This indicates that the inner layer on HR3C can provide a better protection while the

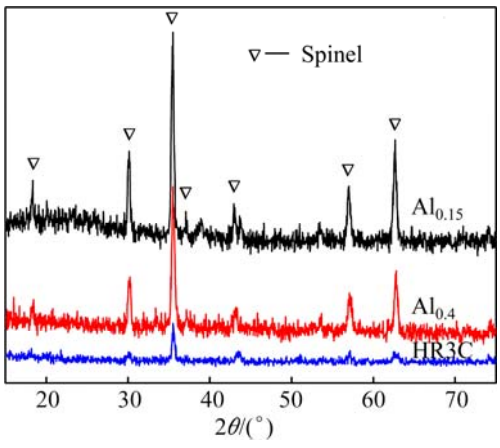

Fig. 11 XRD patterns for $Al_{0.15}$, $Al_{0.4}$ and HR3C after oxidation at 600 °C under 23 MPa for 70 h

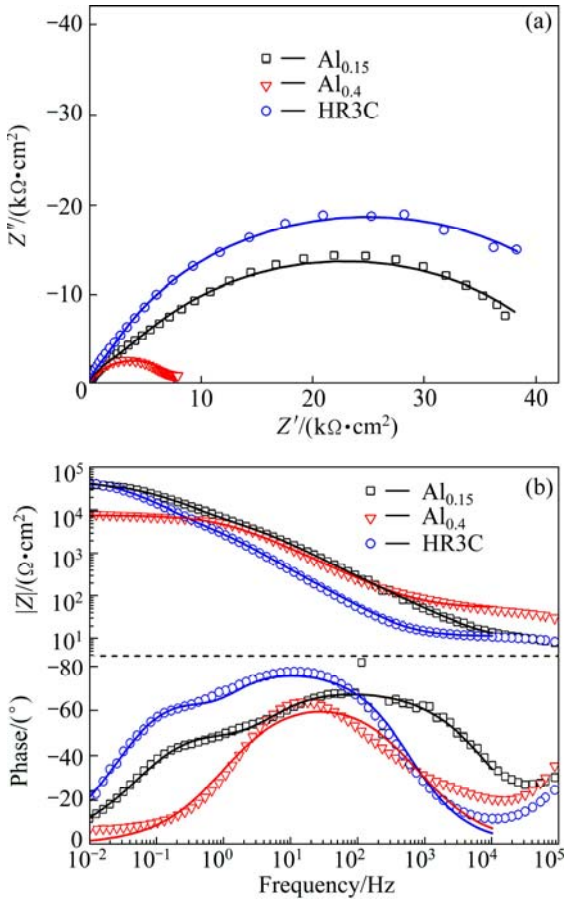

Fig. 12 EIS plots of $Al_{0.15}$, $Al_{0.4}$ and HR3C oxidized at 600 °C under 23 MPa for 70 h

Table 5 Fitting parameters for EIS shown in Fig. 12

Sample	R_1/($\Omega\cdot cm^2$)	Q_1/($\mu F\cdot cm^{-2}$)	n_1	R_2/($\Omega\cdot cm^2$)	Q_2/($\mu F\cdot cm^{-2}$)	n_2
$Al_{0.15}$	1936	9.923	0.858	42222	2.799	0.732
$Al_{0.4}$	7717	4.024	0.754	–	–	–
HR3C	933	157.7	0.995	48151	26.63	0.841

protectiveness of outer layer is poorer compared with $Al_{0.15}$. This result is related to the thickness and compactness of oxide layers on alloys. Although both thicker inner and outer layers are observed on HR3C, the poor compactness of outer layer on this alloy leads to the reduction in R_1; therefore, the R_1 of HR3C is lower than that of $Al_{0.15}$. In addition, the resistances of the inner layer (R_2) on these two alloys are significantly higher than that of outer layer (R_1), revealing that the anticorrosive protection is predominantly provided by the inner layer. Besides, the highest R_1 of $Al_{0.4}$ is correlated with the highest thickness of the single layer in comparison with the inner layers of the other two alloys.

Figure 13 shows the comparison of the polarization curves for substrate and $Al_{0.15}$, $Al_{0.4}$ and HR3C oxidized at 600 °C under 23 MPa for 70 h. The parameters from polarization curves are summarized in Table 6.

Comparing the polarization results of these three substrates, the R_p of HR3C is much higher compared with those of $Al_{0.15}$ and $Al_{0.4}$. It may be attributed to the higher chromium content of HR3C [29]. On the other hand, the R_p of the oxides formed on the three alloys shows a different trend as follows: R_p of the oxides on HR3C is lower than that on $Al_{0.15}$ but higher than that on $Al_{0.4}$. These polarization parameters permit to conclude that the oxides formed on $Al_{0.15}$ can provide the best oxidation protection while that on $Al_{0.4}$ will provide the worst protection. This result is related to the compactness and structure of oxide film. Compared with $Al_{0.15}$, the poor compactness and obvious localized spallation of the oxide film on HR3C result in the poor protectiveness although a thicker oxide film forms. In contrary, for HR3C and $Al_{0.4}$, the protectiveness of oxide film is mainly affected by its structure. As a consequence of single oxide layer on $Al_{0.4}$, the number of interface is reduced. This leads to the energy required for Cl^- ion movement across the interface with freedom is lower; therefore, the single oxide film on $Al_{0.4}$ fails to provide a good protection compared with HR3C with duplex film. Besides, the smaller thickness of the oxides on HR3C is another possible factor resulting in its lower R_p.

4 Conclusions

1) The oxide films formed on $Al_{0.15}$ and HR3C show a duplex layer structure with a Fe_3O_4 outer layer and a

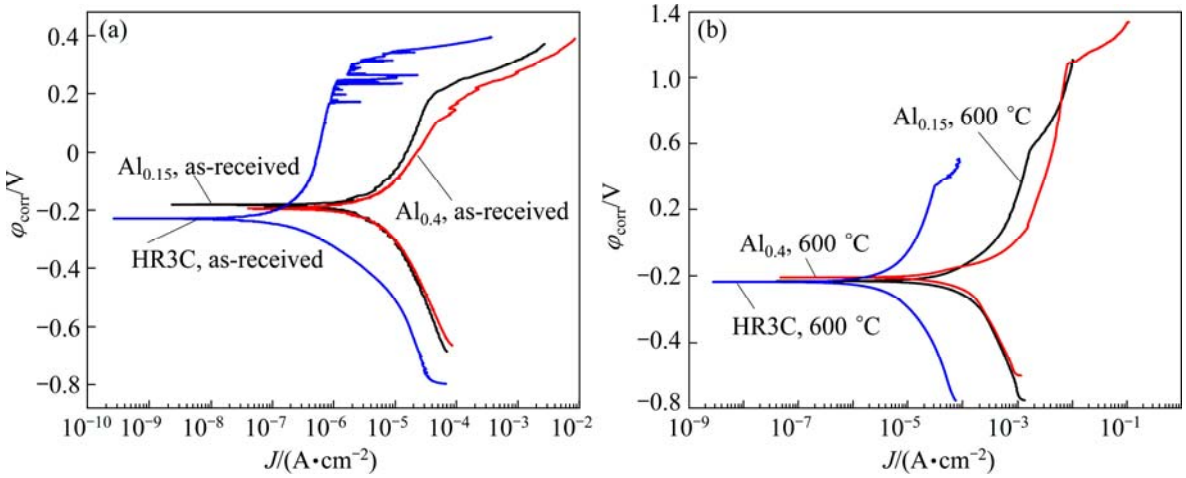

Fig. 13 Polarization curves for substrates (a), and $Al_{0.15}$, $Al_{0.4}$ and HR3C oxidized at 600 °C under 23 MPa for 70 h (b)

Table 6 J_{corr}, φ_{corr} and R_p from polarization curves shown in Fig. 10

Sample	Temperature/°C	J_{corr}/($\mu A\cdot cm^{-2}$)	φ_{corr}/mV	b_c/(mV·dec^{-1})	b_a/(mV·dec^{-1})	R_p/(k$\Omega\cdot cm^{-2}$)
Substrate		1.187	−182.1	137.6	127.7	24.23
$Al_{0.15}$	600	6.013	−234.0	407.8	528.4	16.62
Substrate		8.696	−195.2	483.8	389.2	10.77
$Al_{0.4}$	600	19.61	−207.6	91.91	115.6	1.134
Substrate		0.1314	−228.9	81.30	260.0	204.7
HR3C	600	10.22	−229.3	433.8	435.7	9.236

$FeCr_2O_4$ inner layer while the oxide film on $Al_{0.4}$ mainly consists of a single $FeCr_2O_4$ layer. Compared with the oxide film on HR3C, thinner oxide films with smaller size of oxide particles are realized on $Al_{0.15}$ and $Al_{0.4}$, indicating a superior oxidation resistance of $Al_{0.15}$ and $Al_{0.4}$ to HR3C steel.

2) Electrochemical test results reveal that surface oxide films greatly affect the electrochemical corrosion behavior of the oxidized alloys in 3.5% NaCl solution. The relatively high corrosion resistance of oxidized $Al_{0.15}$ and HR3C is attributed to the formation of thick and multi-layer oxides.

References

[1] YEH J W, CHEN S K, LIN S J, GAN J Y, CHIN T S, SHUN T T, TSAU C H, CHANG S Y. Nanostructured high-entropy alloys with multiple principal elements: Novel alloy design concepts and outcomes [J]. Advanced Engineering Materials, 2004, 6: 299−303.

[2] GREER A L. Confusion by design [J]. Nature, 1993, 366: 303−304.

[3] ZHOU Y J, ZHANG Y, WANG F J, WANG Y L, CHEN G L. Effect of Cu addition on the microstructure and mechanical properties of $AlCoCrFeNiTi_{0.5}$ solid−solution alloy [J]. Journal of Alloys and Compounds, 2008, 466: 201−204.

[4] CHEN Y Y, DUVAL T, HUNG U D, YEH J W, SHIH H C. Microstructure and electrochemical properties of high entropy alloys—A comparison with type-304 stainless steel [J]. Corrosion Science, 2005, 47: 2257−2279.

[5] HUANG Y S, CHEN L, LUI H W, CAI M H, YEH J W. Microstructure, hardness, resistivity and thermal stability of sputtered oxide films of $AlCoCrCu_{0.5}NiFe$ high-entropy alloy [J]. Materials Science and Engineering A, 2007, 457: 77−83.

[6] SENKOV O N, SENKOVA S V, DIMIDUK D M, WOODWARD C, MIRACLE D B. Oxidation behavior of a refractory $NbCrMo_{0.5}Ta_{0.5}TiZr$ alloy [J]. Journal of Materials Science, 2012, 47: 6522−6534.

[7] LIU C M, WANG H M, ZHANG S Q, TANG H B, ZHANG A L. Microstructure and oxidation behavior of new refractory high entropy alloys [J]. Journal of Alloys and Compounds, 2014, 583: 162−169.

[8] LI C, LI J C, ZHAO M, JIANG Q. Effect of aluminum contents on microstructure and properties of $Al_xCoCrFeNi$ alloys [J]. Journal of Alloys and Compounds, 2010, 504(S): s515−s518.

[9] DU Y Y, LU Y P, LI T J, WANG T M, ZHANG G L. Effect of aluminium content of $Al_xCrFe_{1.5}Ni_{0.5}$ multiprincipal alloys on microstructure and alloy hardness [J]. Materials Research Innovations, 2011, 15: 107−110.

[10] YEH J W. Recent progress in high-entropy alloys [J]. Annales De Chimie—Science des Materiaux, 2006, 31: 633−648.

[11] STELLWAG B. The mechanism of oxide film formation on austenitic stainless steels in high temperature water [J]. Corrosion Science, 1998, 40: 337−370.

[12] ZHONG X Y, HAN E H, WU X Q. Corrosion behavior of Alloy 690 in supercritical water [J]. Corrosion Science, 2009, 51: 1069−1072.

[13] CHEN Hu-kui, GONG Zan-fang. Oxidation behaviour of molten ZK60 and ME20 magnesium alloys with magnesium in 1,1,1, 2-tetrafluoroethane/air atmospheres [J]. Transactions of Nonferrous Metals Society of China, 2012, 22(12): 2898−2905.

[14] ZHANG Hai-jun, SUN Jian-feng, ZHOU Yue-bo. Cyclic oxidation and hot corrosion of Al_2O_3 or Y_2O_3-dispersed low-temperature chromizing coating [J]. Transactions of Nonferrous Metals Society of China, 2013, 23(10): 2923−2928.

[15] SUN H, WU X Q, HAN E H. Effects of temperature on the oxide film properties of 304 stainless steel in high temperature lithium borate buffer solution [J]. Corrosion Science, 2009, 51: 2840−2847.

[16] WANG W R, WANG W L, WANG S C, TSAI Y C, LAI C H, YEH J W. Effects of Al addition on the microstructure and mechanical property of $Al_xCoCrFeNi$ high-entropy alloys [J]. Intermetallics, 2012, 26: 44−51.

[17] ISHIDA K, WADA Y, TACHIBANA M, HOSOKAWA H, NAKAMURA M. Effects of noble metal deposition upon corrosion behavior of structural materials in nuclear power plants (I): Effect of noble metal deposition with an oxide film on type 304 stainless steel under simulated hydrogen water chemistry condition [J]. Journal of Nuclear Science and Technology, 2005, 42: 799−808.

[18] MIYAZAWA T, TERACHI T, UCHIDA S, TSUKAD T, SATOH Y, WADA Y, HOSOKAWA H. Effects of hydrogen peroxide on corrosion of stainless steel (V): Characterization of oxide film with multilateral surface analyses [J]. Journal of Nuclear Science and Technology, 2006, 43: 884−895.

[19] LIN C H, DUH J G. Corrosion behavior of $(Ti−Al−Cr−Si−V)_xN_y$ coating on mild steels derived from RF magnetron sputtering [J]. Surface Coating Technology, 2008, 203: 558−561.

[20] YIN K J, QIU S Y, TANG R, ZHANG Q, ZHANG L F. Corrosion behavior of ferritic/martensitic steel P92 in supercritical water [J]. Journal of Supercritical Fluids, 2009, 50: 235−239.

[21] HUANG P K, YEH J W, SHUN T T, CHEN S K. Multi-principal-element alloys with improved oxidation and wear resistance for thermal spray coating [J]. Advanced Engineering Materials, 2004, 6: 74−78.

[22] YEH J W, CHEN S K, GAN J Y, LIN S J, CHIN T S, SHUN T T, TSAU C H, CHANG S Y. Formation of simple crystal structures in solid-solution alloys with multi-principal metallic elements [J]. Metallurgical and Materials Transactions A, 2004, 35: 2533−2536.

[23] TONG C J, CHEN S K, YEH J W, SHUN T T, TSAU C H, LIN S J, CHANG S Y. Microstructure characterization of $Al_xCoCrCuFeNi$ high-entropy alloy system with multi-principal elements [J]. Metallurgical and Materials Transactions A, 2005, 36: 881−893.

[24] WANG F J, ZHANG Y, CHEN G L. Atomic packing efficiency and phase transition in a high entropy alloy [J]. Journal of Alloys and Compounds, 2009, 478: 321−324.

[25] TANG S, ZHU S, TANG X, PAN H, CHEN X, XIANG Z D. Influence of Al on scale formation and growth kinetics of 10 wt.% Cr creep resistant ferritic steels at 650 °C in air [J]. Corrosion Science, 2014, 80: 374−382.

[26] ZHANG Nai-qiang. Research on oxide scale growth mechanism of boiler tube in power plant exposed to supercritical water with dissolved oxygen [D]. Baoding: School of Energy, Power and Mechanism Engineering, North China Electric Power University, 2012. (in Chinese)

[27] SAUNDERS S R J, MONTEIRO M, RIZZO F. The oxidation behaviour of metals and alloys at high temperatures in atmospheres containing water vapour: A review [J]. Progress in Materials Science, 2008, 53: 775−837.

[28] ONAL K, MARIS-SIDA M C, MEIER G H, PETTIT F S. Water vapor effects on the cyclic oxidation resistance of alumina forming alloys [J]. Materials at High Temperatures, 2003, 20: 81−91.

[29] QIAN Y H, NIU D, XU J J, LI M S. The influence of chromium content on the electrochemical behavior of weathering steels [J]. Corrosion Science, 2013, 71: 72−77.

高熵合金 $Al_xCoCrFeNi(x=0.15, 0.4)$ 在超临界水中的氧化行为及其与 HR3C 钢的比较

刘宜萱，程从前，尚建路，王 锐，李 朋，赵 杰

大连理工大学 材料科学与工程学院，大连 116085

摘 要：研究高熵合金 $Al_xCoCrFeNi(x=0.15, 0.4)$在 550、600 °C 超临界水中的氧化行为，并与 HR3C 钢进行对比。研究发现，所有合金表面的氧化膜均由$(Fe,Cr)_3O_4$组成。与 HR3C 钢相比，$Al_{0.15}CoCrFeNi$ 和 $Al_{0.4}CoCrFeNi$ 表面氧化膜较薄，氧化物颗粒较小，其抗氧化性能较好。电化学实验结果表明，氧化后的合金在 3.5% NaCl 溶液中的腐蚀行为受其表面氧化膜的影响。氧化后的 $Al_{0.15}CoCrFeNi$ 和 HR3C 具有较优的耐蚀性，这与其表面生成较厚的双层氧化膜有关。

关键词：高熵合金；高温氧化；极化；电化学阻抗谱(EIS)

(Edited by Xiang-qun LI)